Coupling brain cerebrovascular oscillations and CSF flow during wakefulness: An fMRI study

Running Title: Brain hemodynamic and CSF flow during wakefulness

Ho-Ching (Shawn) Yang[1], Ben Inglis[2], Tom Talavage[3], Vidhya Vijayakrishnan Nair[1], Jinxia (Fiona) Yao[1], Bradley Fitzgerald[4], Amy J. Schwichtenberg[5], and Yunjie Tong[1,*]

[1]Weldon School of Biomedical Engineering, Purdue University, West Lafayette, IN, 47907, USA
[2]Helen Wills Neuroscience Institute, University of California, Berkeley, CA 94720, USA
[3]Department of Biomedical Engineering, University of Cincinnati, OH, 45221, USA
[4]School of Electrical and Computer Engineering, Purdue University, West Lafayette, IN, 47907, USA
[5]Department of Human Development and Family Studies, College of Health and Human Sciences, Purdue University, West Lafayette, IN, 47907, USA

Corresponding author email: tong61@purdue.edu

Number of pages: 29
Number of figures: 6
Number of words for abstract: 194
Number of words for introduction: 553
Number of words for discussion: 1407

Author contribution

Yunjie Tong, Ho-Ching (Shawn) Yang, and Ben Inglis conceived of the presented idea and developed the theory. Ho-Ching (Shawn), Vidhya Vijayakrishnan Nair and Jinxia (Fiona) Yao performed the computations and verified the analytical methods. All authors provided critical feedback and helped shape the research, analysis and manuscript.

Conflict of interest

The authors have no conflict of interest.

Acknowledgements

This work was supported by the National Institutes of Health, Grants S10 grant (S10 OD012336 - 3T MRI Scanner dedicated to Life Sciences Research PI: Ulrike Dydak). Indiana CTSI Core Facility Grant.

Abstract

Cerebral spinal fluid (CSF) plays an important role in the clearance of metabolic waste products from the brain, yet the driving forces of CSF flow are not fully understood. It is commonly believed that CSF flow is facilitated by the blood vessel wall movements (i.e., hemodynamic oscillations) in the brain. A coherent pattern of low frequency hemodynamic oscillations and CSF flow was found recently during non-rapid eye movement sleep (NREM) sleep via functional MRI. However, questions remain regarding 1) the explanation of coupling between hemodynamic oscillations and CSF flow using fMRI signals; 2) the existence of the coupling during wakefulness; 3) the direction of CSF flow. In this resting state fMRI study, we proposed a mechanical model to explain the coupling between hemodynamics and CSF flow through the lens of fMRI. We found that the observed delays between these two signals match those predicted by the model. Moreover, by conducting separated fMRI scans of the brain and neck, we confirmed the low frequency CSF flow at 4th ventricle is bidirectional. Our finding also demonstrates that CSF flow is facilitated by hemodynamic oscillations mainly in the low frequency range, even when the individual is awake.

Significance

Functional MRI has been used to study the coupling between low-frequency hemodynamic oscillations and CSF inflow in the brain during sleep. However, the question remains of how to interpret the coupling using fMRI signal. This study proposed a mechanical model to explain the coupling between hemodynamics and CSF flow through fMRI. By conducting separated fMRI scans covering head and neck during wakefulness, we found the 1) low-frequency hemodynamic oscillation was dominated driving force of CSF dynamics; 2) low-frequency CSF flow at fourth ventricle is bidirectional; 3) the coupling between hemodynamics and CSF flow exists during

wakefulness. This study provides novel physiological perspectives for clearance mechanism in the brain, which is crucial in understanding neurodegenerative diseases.

1. Introduction

The glymphatic system plays an important role in the clearance of metabolic waste products in the extracellular interstitial space (Iliff et al., 2013; Xie et al., 2013) and the distribution of homeostasis-sustaining compounds (e.g., glucose) in the brain (Aalling et al., 2017). Recent advancements of the glymphatic system highlight its role in the development of neurodegenerative diseases. Unlike blood flow, which is driven by the heart pumping, CSF does not appear to have an engine to generate flow. Thus, CSF flow has been assumed to be mostly facilitated by the mechanisms associated with vessel wall movement (blood flow), including vasomotion (Mestre et al., 2018; van Veluw et al., 2020), pulsation (Chen et al., 2015), and/or inspiratory thoracic pressure changes (Dreha-Kulaczewski et al., 2015, 2017).

Several magnetic resonance imaging (MRI) techniques have been used to investigate CSF flow in the brain, including 1) phase-contrast imaging (Matsumae et al., 2019); 2) velocity density imaging (Feinberg and Mark, 1987); 3) time-spatial labeling inversion pulse imaging (Yamada et al., 2008); and 4) 4D flow MRI (Jaeger et al., 2020). These imaging techniques were often used to detect the direction of CSF motion within a single cardiac/respiration cycle. However, they cannot reveal real-time CSF flow over a longer period or bulk flow.

Recently, Fultz et al used a fast EPI sequence (TR<400ms) to study bulk CSF flow (Fultz et al., 2019). They ingeniously placed the edge of the imaging volume (the first slice) at the fourth ventricle, which allows them to measure the flow of CSF using the inflow effect (Duyn et al.,

1994) in the fMRI signal (rather than blood-oxygen-level-dependent (BOLD) contrast). They discovered a coherent pattern of oscillating electrophysiological, hemodynamic, and CSF dynamics that appears during non–rapid eye movement (NREM) sleep. Their results suggested the coupling between CSF inflow and the hemodynamic signal is related to waste clearance from the brain during sleep. While still a qualitative approach to measurement of CSF flux, the advantages of the fast EPI approach are obvious. First, the fast EPI sequence is widely available, and the data processing is straightforward. Second, through simultaneous recording, coupling between brain hemodynamics and CSF flow, which is crucial in understanding the fundamental driving mechanism of CSF flow, can be examined. In this case, hemodynamics and CSF flow can be assessed by BOLD and in-flow contrast of fMRI respectively.

While effective and innovate, the study by Fultz et al. raises several scientific questions. First, they reported correlations between the derivative of the averaged fMRI signal in gray matter with CSF inflow signal; however, no detailed mechanistic explanation was given. Second, similar coupling was not fully explored during the awake state. Last, due to the limitation of the scan parameters, their method could only assess the inflow of CSF to the brain, but not the outflow from the fourth ventricle (i.e., to the neck). The difference between these two bulk flow rates would be indicative of the overall CSF flux.

This study was designed to address these questions. First, we proposed a simple mechanical model to explain the relationships between CSF movement and hemodynamic fluctuations in fMRI signal. Second, we investigated the coupling between brain hemodynamics and CSF flow during the awake state by an fMRI scan. Last, an additional fMRI scan was employed to assess CSF outflow and compare it with the brain hemodynamics.

2. Method

2.1 Model

The brain is in a rigid container. As a result, the volumes of the constituents (blood, CSF, and brain parenchyma) consistently fluctuate to maintain the total volume needed for proper internal pressure—i.e., the Monro-Kellie doctrine (Mokri, 2001). According to this doctrine, transfer of movements from the arterial walls into the surrounding tissue will eventually cause CSF flow into and out of the spinal canal (Delaidelli and Moiraghi, 2017; Dreha-Kulaczewski et al., 2018; Spijkerman et al., 2019). Multiple mechanisms cause arterial wall oscillations at various frequencies, such as cardiac pulsation (1Hz) and vasomotion (<0.1Hz). They have all been shown to produce flow of CSF (Chen et al., 2015; Dreha-Kulaczewski et al., 2015, 2017; Mestre et al., 2018; van Veluw et al., 2020). However, how to interpret the coupling between hemodynamic and CSF flow changes using fMRI signal is still not clear.

Here, we offer a general model that explains the coupling between these fMRI signals (hemodynamic and CSF flow changes). The model is based on the hypothesis that the accumulative effects of vessel dilations and contraction (pulsation, vasomotion) will exert force on the walls of ventricles, especially the lateral ventricles (no blood vessel in the ventricles), forcing CSF in and out of the fourth ventricle at the bottom (see Figure 1). In this model, the global mean of fMRI signals (GMS) is used as a surrogate signal to indirectly assess the accumulative effects of vessel dilations and contractions in the brain (Vigneau-Roy et al., 2014; Yang et al., 2019). In Figure 1, we simulated volume changes in blood vessels and their consequential CSF flow observed at the fourth ventricle. In detail, the blood-rich region will expand because of vessel dilation. This will compress the volume of the lateral ventricle, forcing CSF out of the brain. The reverse happens when the vessels contract. However, the key point here is that CSF flow only happens at the transitions, during which the cerebral blood volume (CBV) changes (as shown by

the arrows in figure 1). When CBV is stabilized, no force is exerted on the ventricular wall, thus no flow of CSF. Therefore, the model predicts CSF outflow at the fourth ventricle during CBV transition from low to high, and CSF inflow during CBV transition from high to low. Since GMS of fMRI roughly represents CBV in the brain, the transitions are accurately captured by the derivative of GMS ($\frac{d}{dt}$(GMS)), not GMS itself.

Based on this model, we have several predictions (Figure 1): 1) CSF inflow signal should be negatively correlated with $\frac{d}{dt}$(GMS); 2) since CBV change in the brain is the cause of CSF flow and the brain is not a rigid body, CSF inflow signal should lag behind $\frac{d}{dt}$(GMS); 3) CSF outflow signal (towards the neck) should be positively correlated with $\frac{d}{dt}$(GMS) and lag behind $\frac{d}{dt}$(GMS) for the same reason as in (2). To assess these predictions, we have conducted the following studies using specially designed scan locations and sequences.

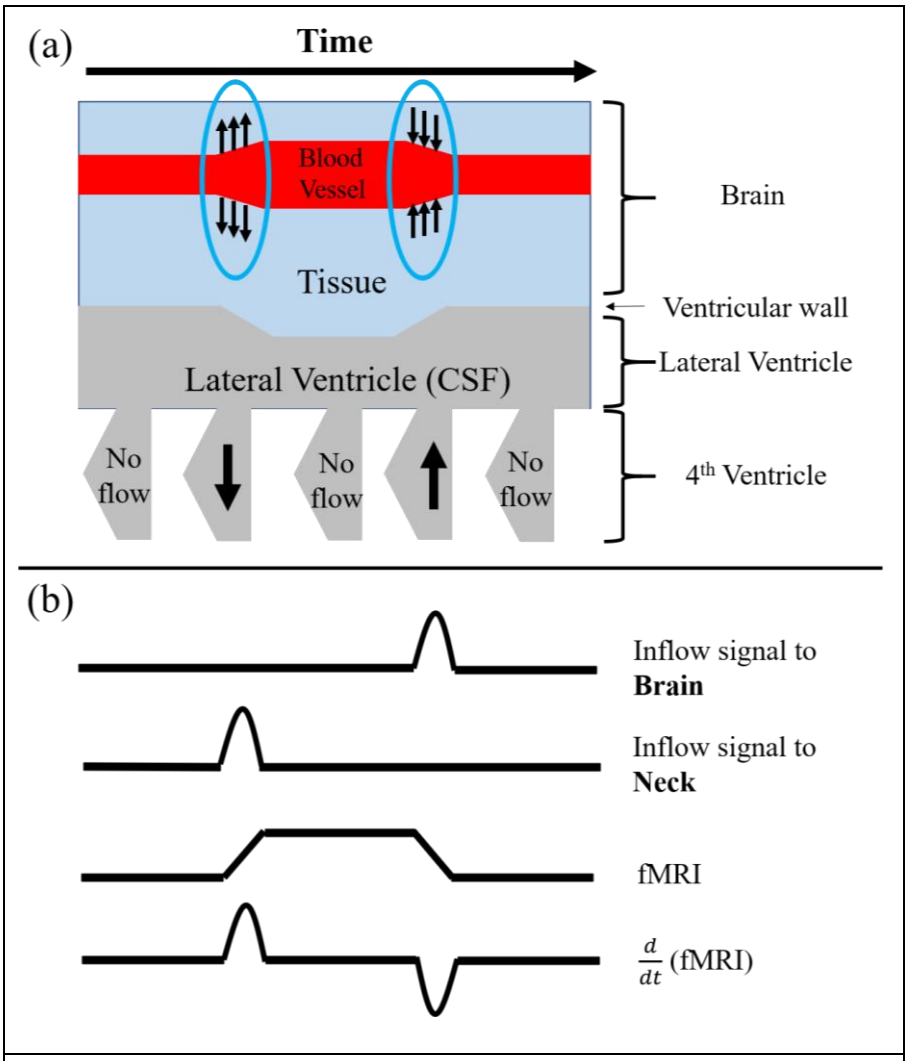

Figure 1. The brain model and its corresponding fMRI signals measured at the fourth ventricle and brain (global mean signal). (a) The model illustrates the temporal changes in vessel volume with the corresponding effects on the lateral ventricle shape and CSF flow at the fourth ventricle. Blue circles show periods of vessel volume change (i.e., transition). Arrows in the blue circles point to the direction of vessel wall movement. (b) Corresponding signals and their derivatives observed at the fourth ventricle, brain (global mean signal). The flow signal is from the inflow ('time of flight') effect. The brain fMRI signal is from the BOLD effect.

2.2 Protocol

2.2.1 Structure Scans

This study was approved by the Purdue University Institutional Review Board. Informed consent was obtained from all participants. Ten healthy individuals (5 female, 5 male, age range 23-30 years) were recruited. MRI data were obtained using a 3T SIEMENS MRI scanner (Magnetom Prisma, Siemens Medical Solutions, Erlangen, Germany) and a 64-channel head coil. Each participant has one T1-weighted, one T2-weighted, and two functional scans. For T1-weighted scans, multiplanar rapidly acquired gradient-echo (MPRAGE) structural images were acquired with the following parameters (TR/TE: 2300/2.26 ms, 192 slices per slab, flip angle: 8 deg, resolution: 1.0mm × 1.0mm × 1.0mm). Parameters for T2-weighted scans were as follows (TR/TE: 2800/409 ms, 208 slices per slab, resolution: 0.8mm × 0.8mm × 0.7mm). Since this study has two fast EPI MRI scans covering the head and neck respectively (Figure. 2), long T1-w and T2-w images covering the head and neck were taken.

2.2.2 EPI scans

The functional resting state (RS) scans were acquired using a multiband echo-planar imaging sequence (FOV = 230 mm, acquisition matrix = 92 × 92, 48 slices, voxel size = 2.5 × 2.5 × 2.5 mm^3, TR/TE = 440/30.6 ms, echo-spacing=0.51 ms, flip angle = 35°, hyperband acceleration factor = 8, multi-slice mode: interleaved). Participants were instructed to stay awake during the RS scans. CSF inflow captured by fast EPI sequence was discussed in detail in Fultz et al (Fultz et al., 2019). In short, as fresh fluid particles (not experienced radiofrequency pulses) move into the imaging volume, they induce higher signal intensity (i.e., inflow effect). To capture the inflow effect in both directions in the fourth ventricle, two 5-minute RS scans with different regions of

interest were included. Both scans are positioned with the edge of the volume placed at bottom of the fourth ventricle (see figure 2 (a,b)), with one scan extending upward toward the top of the head (i.e., brain scan) and another scan extending downward into the neck (i.e., neck scan). As result, CSF inflow to the brain can be assessed by the brain scan, while CSF outflow from the brain can be assessed by the neck scan (i.e., considered as "inflow" to the scan volume that is the neck), under the assumption that flow sensitivity in the opposite directions can be ignored due to steady-state excitation in those slices either above or below the slice of interest. The slice of interest, at the fourth ventricle, was consistently acquired firstly in the TR.

2.3 Data processing

2.3.1 CSF flow signals

All MR data were processed using FSL (FMRIB Expert Analysis Tool, v6.01; Oxford University, UK (Jenkinson et al., 2012)) and MATLAB. For analysis of CSF flow dynamics, a voxel in the fourth ventricle in the edge slice of the EPI data was identified with help of the T1-weighted image (registered onto the EPI data). The time series of the voxel was extracted to represent CSF flow. For CSF inflow, the signal was extracted from the bottom EPI slice of the head scan as shown in figure 2 (a, c, e). For CSF outflow, the signal was extracted from the top slice of the neck scan as shown in figure 2 (b, d, f). We hereafter refer to these two signals as "CSF inflow" and "CSF outflow", even though they both stem from the inflow effect in fMRI.

2.3.2 Preprocessing

Since motion correction cannot be accurately performed on edge slices (given that tissue moves in and out of the imaging volume), only the slice-timing correction was performed prior to CSF flow signal extraction (Fultz et al., 2019). Then RS-fMRI data were preprocessed with the

steps recommended by Power et al. (Power et al., 2014): 1) slice-timing correction (FSL *slicetimer*) 2) motion correction (FSL *mcflirt*) and 3) spatial smoothing with a full width at half maximum (FWHM) of 5 mm isotropic Gaussian kernel.

2.3 Data analysis

Segmentation was performed on the structural image. Several masks were made to investigate the coupling between CSF inflow signal and fMRI signal from these segmentations (Figure 2 (g)). First, anatomical masks for gray matter, white matter, and CSF were made using an automated segmentation program (FSL *fast*) (Zhang et al., 2001). Second, we identified large veins in the neck (i.e., internal jugular veins (IJVs)) and made corresponding masks (Figure 2 (h)). In a previous RS fMRI study, we found consistent positive correlations (>0.8) between GMS of the brain and the fMRI signal from the IJVs (Tong et al., 2019). Therefore, here we used the fMRI signal from the IJVs as a surrogate signal of GMS (of the brain) in the neck scan. Detailed information about IJV mask identification can be found in a previous publication (Tong et al., 2019).

After extraction, the fMRI signals, including CSF flow signals (fourth ventricle), GMS from gray matter, white matter and CSF, and signals from big veins (IJV), were first linearly detrended, and then band-pass filtered (0.01 to 0.1 Hz) using a zero delay, fourth-order Butterworth filter to extract the low frequency oscillations (LFO). Cross correlations (MATLAB *xcorr*, lag range =$\pm$ 45 seconds) were calculated between (1) $\frac{d}{dt}$(GMS) and CSF inflow signals, and (2) $\frac{d}{dt}$(IJV) and CSF outflow signals. The maximal cross correlation coefficients (MCCC) and the corresponding delays were calculated for all the research participants. Moreover, to assess the coupling between CSF inflow signal with the whole brain and understand any spatial relationship,

CSF inflow signal was cross-correlated with $\frac{d}{dt}$(fMRI signal) for every voxel in the brain. The MCCC and delay maps were derived for each participant, and the average was also calculated.

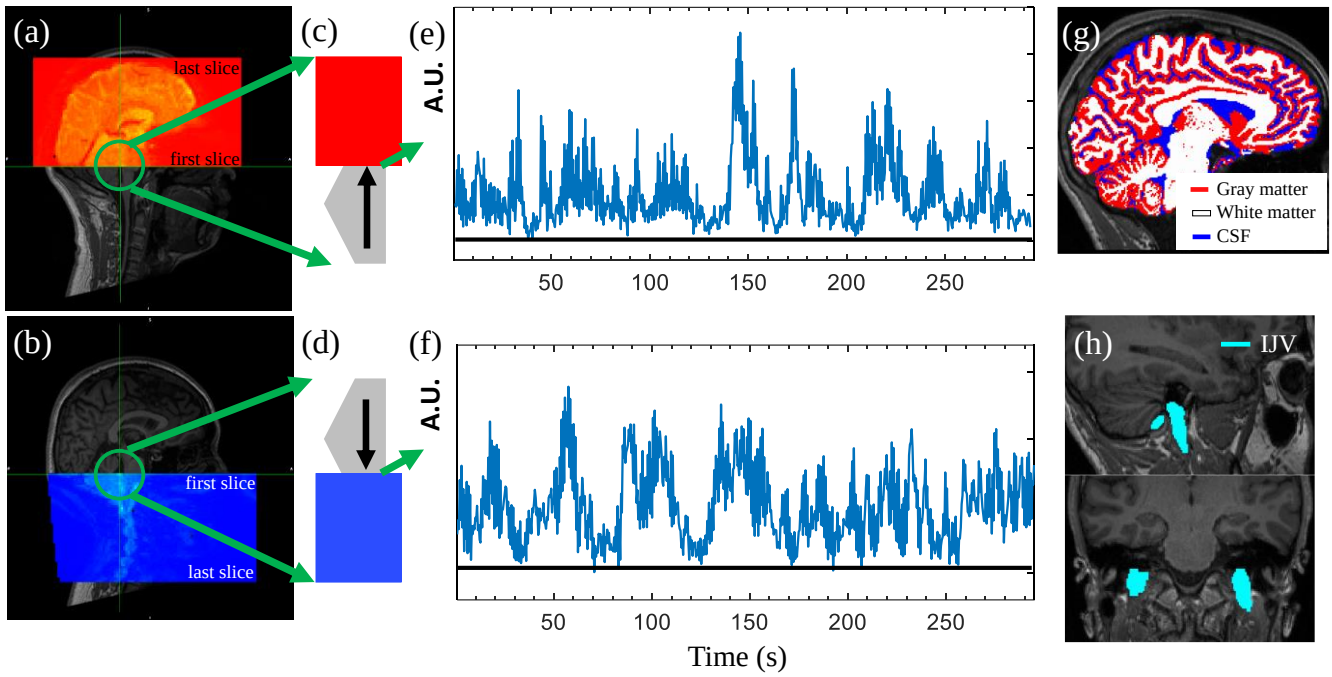

Figure 2. The scan designs and corresponding CSF flow signals. The scan volumes used in the brain scan (a) and the neck scan (b). Enlarged sections illustrate the "inflow effects" in two scans. In the brain scan (c), the signal detected at the first slice (green circle) represents CSF flow into the brain. In the neck scan (d), the signal detected at the first slice (green circle) represents CSF flow into the neck. The corresponding unfiltered, raw time series extracted from the green circles in (a) and (b), are shown in (e) and (f) respectively. They represent CSF flow signal to the brain (e) and to the neck (f). Both show large slow oscillations in addition to rapid oscillations due to cardiac pulsation. (g) Brain segmentations used to identify gray matter, white matter, and CSF. (h) Blood vessel segmentations in the neck to identify internal jugular veins (IJV).

3. Results

3.1 CSF flow during wakefulness

Figure 2 (e) shows an example CSF flow signal obtained from the brain scan. First, it shows that during an awake state, CSF inflow signals are clearly detectable. Second, CSF outflow (Figure 2 (f)) was clearly captured in the neck scan, as predicted by the model, indicating that the low frequency CSF flow is also bi-directional. Note that CSF flow signals are unidirectional in each scan, leading to a flat baseline after detrending (black lines in figure 2 (e) and (f)). This is because the signal originates from the inflow effect which is sensitive to CSF flow in one direction only (i.e., into the scan volume). When CSF flows in the opposite direction, there is no inflow signal enhancement (i.e., flat). Furthermore, from figure 2 (e, f), the area under CSF signal fluctuation curves should reflect the amount of CSF flowing in each direction during the period of scan.

3.2 CSF flow signal and $\frac{d}{dt}(\mathrm{GMS})$

Figure 3 displays example low frequency data from one research participant. It shows $\frac{d}{dt}(\mathrm{GMS})$ of the brain and CSF inflow signal in (a-c), and the same participant's $\frac{d}{dt}(\mathrm{IJV})$ and CSF outflow in (d-f). As mentioned, when describing the model, $\frac{d}{dt}(\mathrm{GMS})$ is sensitive to the transitions of CBV in the brain, where a larger signal indicates a faster transition. During these transition times, CSF was forced to flow in and out of the brain (through the fourth ventricle). Specifically, positive signals in $\frac{d}{dt}(\mathrm{GMS})$ related to CSF outflow, while negative signals in $\frac{d}{dt}(\mathrm{GMS})$ related to CSF inflow. As shown in figure 3, CSF inflow signal matched the lower part of $\frac{d}{dt}(\mathrm{GMS})$ in (b) (CSF inflow signal was flipped for demonstration; MCCC= -0.75), while CSF outflow signal matched the upper part of $\frac{d}{dt}(\mathrm{IJV})$ in (e) (MCCC=0.83). Note that, here we used $\frac{d}{dt}(\mathrm{IJV})$ to

represent $\frac{d}{dt}(\mathrm{GMS})$. Thus, CSF outflow signal matched the upper part of $\frac{d}{dt}(\mathrm{GMS})$. Moreover, this result also indicated that $\frac{d}{dt}(\mathrm{GMS})$, unlike CSF flow signal that can only report the flow in one direction, is able to reflect CSF flow in both directions. Last, from the delays, CSF inflow lagged $\frac{d}{dt}(\mathrm{GMS})$ by about 2.2s (Figure 3 (c)). This delay was predicted by the model, indicating CBV changes are likely the "cause" for CSF flow, though maybe not the only one. Similar results in delay were also shown in figure 3 (f). However, CSF outflow signal is leading $\frac{d}{dt}(\mathrm{IJV})$ signal by about 2.2 s. From previous studies, the fMRI signal of IJV lags GMS by about 4 seconds (Tong et al., 2019). After the adjustment for this delay, CSF outflow signal should still be lagging the true $\frac{d}{dt}(\mathrm{GMS})$—i.e., the brain signal—by about 2 seconds, which is consistent with the findings in figure 3 (a-c).

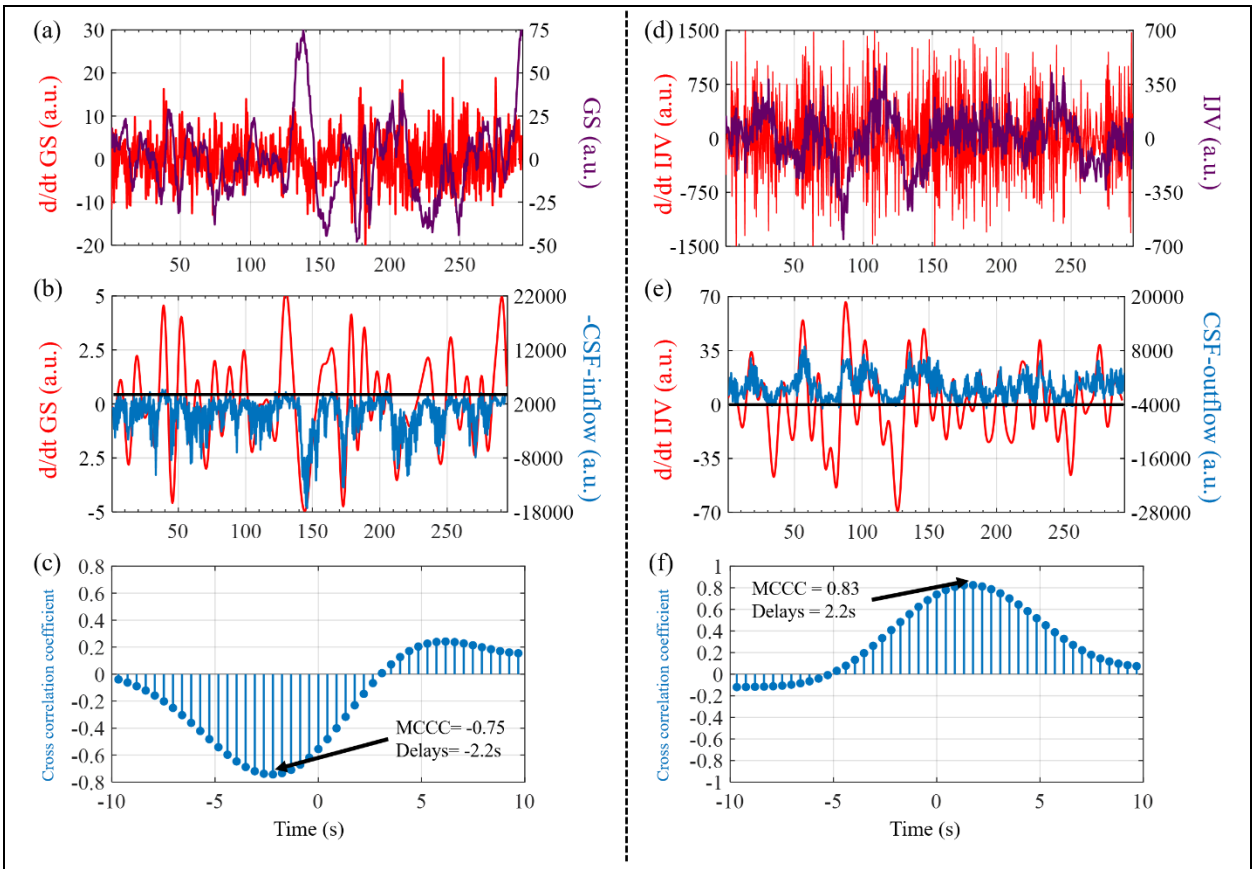

Figure 3. The relationships between GMS of the brain, CSF inflow signal (a-c), averaged IJV signal and CSF outflow signal (d-f) from the same research participant. (a) Time series of GMS in purple and its derivatives ($\frac{d}{dt}$(GMS)) in red. (b) Time series of $\frac{d}{dt}$(GMS) after filtering (0.01~0.1Hz) with the negative raw CSF inflow signal. It shows CSF inflow signal matches the lower part of filtered $\frac{d}{dt}$(GMS). (c) Cross-correlation between filtered $\frac{d}{dt}$(GMS) and CSF inflow shows the $\frac{d}{dt}$(GMS) is ahead of CSF inflow signal with high MCCC (-0.75). (d) Time series of IJV signal in purple and the derivative of IJV ($\frac{d}{dt}$(IJV)) in red. (e) The time series of filtered $\frac{d}{dt}$(IJV) and CSF outflow signal. It shows CSF outflow signal matches the top part of filtered $\frac{d}{dt}$(IJV). (f) Cross-correlation between filtered $\frac{d}{dt}$(IJV) and CSF outflow signal shows $\frac{d}{dt}$(IJV) is

a little behind of CSF outflow signal with high MCCC. GMS: global mean signal. MCCC: maximum cross correlation coefficient. IJV: internal jugular vein.

Figure 4 (a) shows the individual and average results of MCCCs and delay calculated between $\frac{d}{dt}$(GMS) and CSF inflow signal from the brain scans. Here $\frac{d}{dt}$(GMS) was calculated from the gray matter, white matter, and CSF-region in the brain. The MCCCs from all the participants are high for all the tissue types (MCCC for gray matter: -0.76$\pm$0.07; for white matter: -0.69$\pm$0.10; and for CSF: -0.76$\pm$0.07 ($p<10^{-8}$ for all)). The corresponding delays are around -2s—i.e., $\frac{d}{dt}$(GMS) signal is leading CSF inflow signal. Among the three tissue types, $\frac{d}{dt}$(GMS) from gray matter, white matter, and CSF-region led CSF inflow by 2.2$\pm$0.55s, 2.02$\pm$0.69s and 1.36$\pm$0.60s ($p<10^{-4}$ for all), respectively. Figure 4 (b) shows the average results of MCCCs and delays calculated between $\frac{d}{dt}$(IJV) and CSF outflow signal. The averaged MCCC is 0.64$\pm$0.30s ($p<10^{-4}$) with averaged delay of 0.66$\pm$3.39s ($p>0.05$). As we mentioned previously, after adjustment for the delay between fMRI signal of IJV and GMS (~4s), CSF outflow signal should lag the brain signal ($\frac{d}{dt}$(GMS)) by about 2 s (Tong et al., 2017).

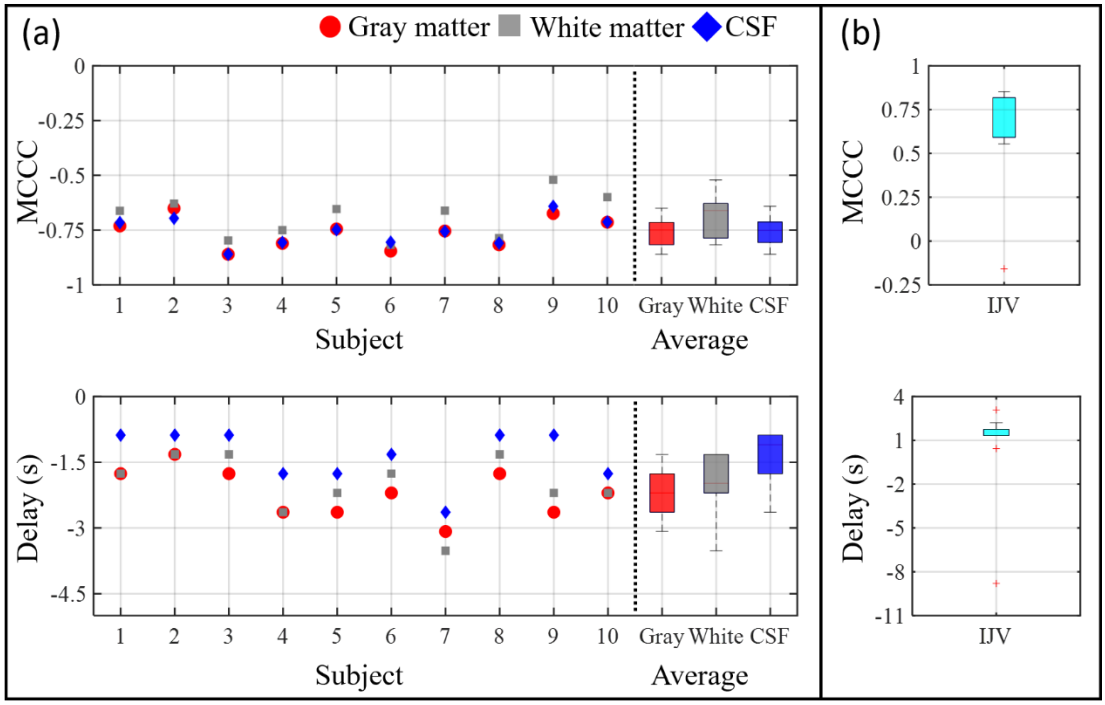

Figure 4. The summary of the cross-correlations between CSF inflow signal and $\frac{d}{dt}$(GMS) from different regions of interest (ROIs). (a) MCCCs and delays between CSF inflow signal and $\frac{d}{dt}$(Gray matter), $\frac{d}{dt}$(White matter), $\frac{d}{dt}$(CSF) in each participant and the averaged result from all participants. All the $\frac{d}{dt}$(GMS) in different ROIs are temporally ahead of CSF inflow signal with high negative MCCCs. (b) Averaged MCCCs and delays between CSF outflow signal and $\frac{d}{dt}$(IJV). All but one have high positive MCCCs and positive delays. GMS: global mean signal. MCCC: maximum cross correlation coefficient. IJV: internal jugular vein.

3.3 Spatial-temporal information of the coupling of CSF inflow with the brain signal

Figure 5 shows the averaged MCCCs and delay maps derived from the voxel-wise cross correlation between CSF inflow signal and $\frac{d}{dt}$(fMRI signal). Negative MCCCs were found in most of the tissue-containing voxels with distributions shown in figure 5 (a). Regions with the highest negative MCCCs are found in the gray matter, especially in high blood density regions such as the visual cortex. It is worth noting that the positive correlations (shown in blue) were found in the voxels next to the lateral ventricles (Figure 5 (a,b)), likely due to partial volume effects.

Negative delays were found in most of the voxels with distributions shown in figure 5 (f). Negative delays indicate that $\frac{d}{dt}$(fMRI signal) is leading CSF inflow signal. This result is consistent with the findings in figures 3 and 4. As we consider the changes in CBV as a cause for "pressure waves", the delay map then represents the propagation of these waves in the brain. From figure 5 (d), we can see that they started from the precentral gyrus, and moved toward the regions surrounding the ventricles (red/yellow in figure 5 (d)). However, a few observations do not fit the proposed model. First, the voxels with the longest delays (red/yellow in figure 5 (d)), which cover much of the extended region from the ventricles into the white matter, do not overlap with the positively correlated voxels in figure 5 (a). Second, the delay values are positive, indicating they lag a few seconds after CSF inflow. Therefore, signals from these voxels still reflect CBV changes, but following CSF inflow, which might indicate there are secondary interactions between CSF inflow and white matter.

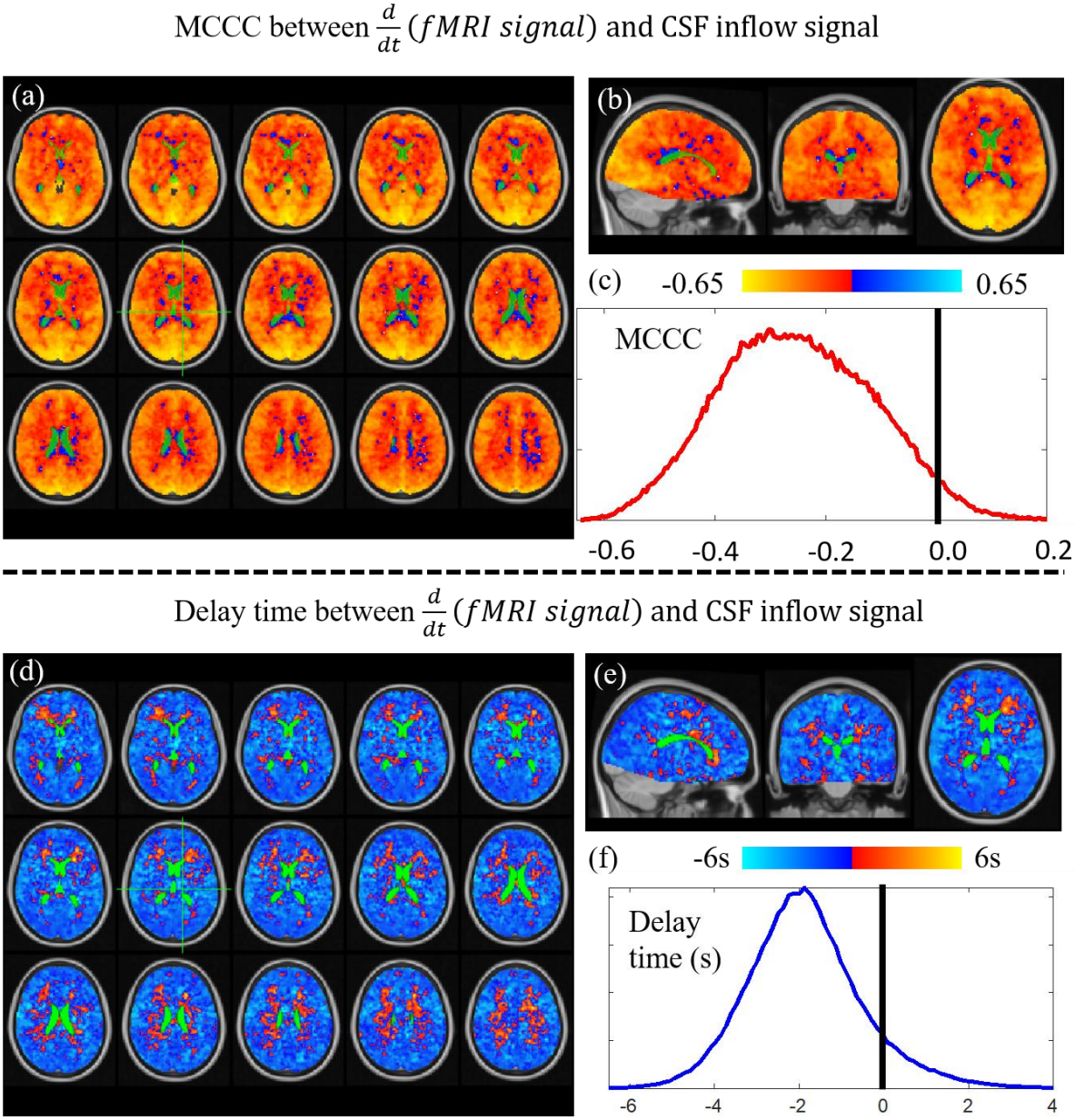

Figure 5. Group average of voxel wise cross-correlation between $\frac{d}{dt}$(fMRI signal) and CSF inflow signal. (a-b) Various views of whole brain MCCCs show that most of the $\frac{d}{dt}$(fMRI signal) in the brain were negatively (red-yellow) correlated with CSF inflow signal. (c) The distribution of MCCCs. (d-e) Various views of whole brain delays show that most of the $\frac{d}{dt}$

(fMRI signal) is ahead of CSF inflow signal. (f) The distribution of the delays. MCCC: maximum cross correlation coefficient.

4. Discussion

This study used a simple model to explain the correlation and delays between $\frac{d}{dt}$(GMS) of fMRI and CSF flow measured at the fourth ventricle. With both brain and neck scans, we validated that CSF flow at low frequencies were bi-directional and found that coupling between the brain hemodynamics and CSF flow exists for awake participants in the supine position.

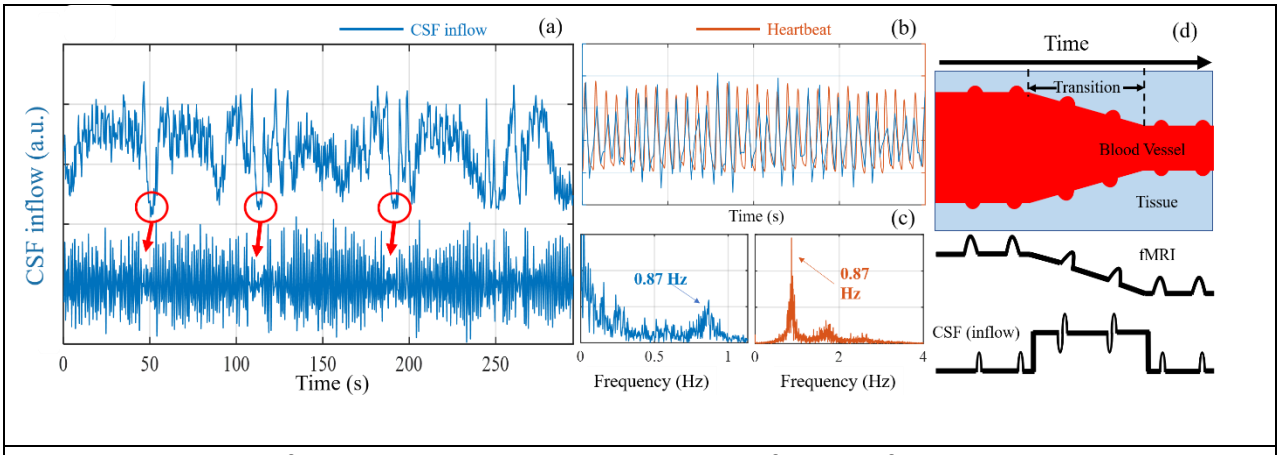

Figure 6 (a) CSF inflow signal (upper panel: raw data of CSF inflow; lower panel: high pass filtered CSF inflow (>0.6Hz) to extract the heartbeat signal). Three red circles represent big drops of CSF inflow, which indicate CSF outflow or no flow. In these periods, smaller amplitudes of heartbeat signals are found (pointed by red arrows). (b) High frequency CSF inflow signal (>0.6Hz, blue) and heartbeat signal recovered from the brain data using "Happy" (Aslan et al., 2019). (c) Power spectrum (arbitrary unit) of CSF inflow signal and power spectrum of heartbeat signal (right). These two panels show that 1) the heartbeat signal can be detected in CSF inflow signal, which matched that of the brain; 2) little or no delay was found in the heartbeat signal in

the brain and that detected in CSF inflow. (d) Model depicts the low-frequency (e.g., vasomotion) and high-frequency (heartbeat) vessel volume changes and their impacts on the fMRI, and CSF inflow signals.

4.1 Possible driving forces for CSF flow

Previous studies have proposed several driving forces for CSF flow, which included 1) cardiac pulsation (Schley et al., 2006), 2) vasomotion (van Veluw et al., 2020), and 3) respiration (Klose et al., 2000; Dreha-Kulaczewski et al., 2017). Some studies demonstrate that pulsation is a driving force for CSF (Schley et al., 2006; Wang and Olbricht, 2011; Iliff et al., 2013). However, others studies used mathematical model to argue that arteriolar pulsation alone are too weak to drive CSF circulation (Asgari et al., 2016; Diem et al., 2017).

Figure 6 (a) is example data of CSF inflow taken from one participant's head scan. It compares the effect of pulsation and slow arteriolar oscillation on CSF inflow. The LFOs are dominant in the signal, and thus are the main contributor to CSF flow. This is further confirmed by the power spectrum of the signal (Figure 6 (c)), in which the heartbeat signal (~0.87Hz) is much smaller than that of LFOs. These LFO signals are associated with arteriolar slow oscillations, such as vasomotion created by rhythmic spontaneous contractions of vascular smooth muscle cells (Diem et al., 2017; Albargothy et al., 2018; Aldea et al., 2019; van Veluw et al., 2020). On the same note, increased ultra-low frequency vasomotion (0.1 Hz) in arterioles was found to increase clearance rate from perivascular space (van Veluw et al., 2020).

To investigate the pulsatile CSF inflow and blood flow, we extracted the full cardiac pulsation waveform from the undersampled brain fMRI scan (Aslan et al., 2019). A section of

reconstructed cardiac waveform is shown in figure 6 (b), together with the cardiac wave derived from CSF inflow signal by high-pass filtering (>0.6 Hz). These two signals match with no clear delays, likely because of the fast-traveling nature of cardiac pulsation.

Based on these findings, we adapted the model in figure 1 by adding the pulsatile oscillations. Thus, the model included both pulsatile and slow arteriolar oscillations on the blood vessels (Figure 6 (d)), in which, the faster and smaller pulsatile changes were added to the slow, bigger low frequency changes. From the model, we can see that 1) inflow will be continuous during the slow transition period (as marked in figure 6 (d)). 2) The pulsations during this period will modulate the inflow speed (not reverse flow direction), thus full scale of the derivative pulsatile signal is "recorded" by the fMRI data. However, for the pulsations happening outside this period, they induced CSF flow in both directions. Therefore, only partial signal (positive derivative pulsatile signal) was "recorded". This explained why the magnitudes of heartbeat-related signals were bigger during the inflow period, and much smaller or invisible otherwise (circles in figure 6 (a)).

In addition to pulsation and vasomotion, several lines of work showed that respiration is instrumental in driving CSF through the aqueduct by real-time phase contrast MRI measurements (Klose et al., 2000; Yamada et al., 2013; Chen et al., 2015; Dreha-Kulaczewski et al., 2015, 2017). Furthermore, Dreha-Kulaczewski et al. proposed that increased CSF flow from caudal to cranial during inspiration was considered compensation of venous blood leaving from head due to lower intrathoracic pressure (Dreha-Kulaczewski et al., 2017). Based on this theory (i.e., pressure), CSF inflow and blood outflow (i.e., vein) should happen simultaneously. however, we can only measure the LFO of CSF outflow and fMRI signal in IJV simultaneously in the neck scan. There are no consistent delays found between these two signals, yet the delay between CSF outflow and $\frac{d}{dt}$(IJV)

was about 2.2s (i.e., CSF leading $\frac{d}{dt}(\mathrm{IJV})$). This result may support the "top model" that the original "engine" for CSF flow is from above, i.e., cerebrovascular oscillation (see Figure 4), instead of the lung. As we discuss in 4.3, cerebrovascular slow oscillations move with blood through the brain slowly (take a few seconds). The oscillations will compress and expand lateral ventricles, which lead to CSF flow observed at the fourth ventricle. The same oscillations will eventually move to the vein and be observed at IJVs.

Our study focused on the LFO of the signal, not the respiration frequency. The natural breathing frequencies of our participant were from 0.2-0.4 Hz (The power spectra of CSF inflow/outflow, GLM signals of all the participants can be found in the supplementary material). Like cardiac pulsation, the power of the respiration signal is much less than that of the LFOs, indicating that the arterial LFO is the dominant force in driving CSF flow, at least in resting state without using any forced/paced breathing protocol. In addition, forced or paced breathing as used in Dreha-Kulaczewski's study might invoke different physiological responses/mechanisms, other than the ones under regular breathing (Dreha-Kulaczewski et al., 2017).

This study and previous research found CSF flowed in both directions through the fourth ventricle (Matsumae et al., 2019). To roughly assess the net flow, we calculated the areas under 1) CSF inflow (from brain scan) and 2) CSF outflow (from neck scan) for each participant (details are in supplementary material). No consistent net flow direction was detected among participants, indicating the net flow was not substantial during the short scan time (i.e., # minutes). It is known that adult only secret 25 ml CSF/hour in the brain (mostly from the choroid plexuses of the lateral ventricles) (Telano and Baker, 2020). The secretion creates a pressure that dictates the direction of CSF flow through the ventricular system to the subarachnoid space (net flow in one direction).

However, due to the small amount, the net flow would be hard to detect during the short period of time with our imaging method.

In summary, though our model explains the underlying mechanism between vessel volume dynamics and CSF flow, it does not discern the causes for the vessel dynamics. It is probable that multiple mechanisms contribute to facilitate CSF flow.

4.2 Ventricular vs. perivascular effects

Unlike fast traveling cardiac pulsation that reaches all the voxels in the brain at almost same time, LFOs in BOLD fMRI (associated with vasomotion or arterial O_2 and CO_2 fluctuations) have been shown to propagate in the brain as the blood flow (Tong et al., 2017) and take up to 5s to transit the brain. The corresponding vessel dilation or pressure wave ($\frac{d}{dt}$(fMRI signal)) is shown to have a clear spatial-temporal pattern in figure 5 (d), moving from an arterial-rich region to the white matter regions, then the vicinities of lateral ventricles in seconds. As a result, the ventricular wall might be compressed continuously and sequentially, not simultaneously as in the case of pulsation. This also explained the delay (1-2s) we observed in the LFO signals of CSF and $\frac{d}{dt}$(fMRI signal), while, not in the cardiac pulsation signals (Figure 6).

It was evident that CSF tracers entered the parenchyma through a periarterial pathway and ex-vivo evidence showed that tracers rapidly exited the brain primarily along central deep veins and the lateral ventral caudal rhinal veins (Nedergaard, 2013; Xie et al., 2013). This offers another pathway of CSF travel through perivascular structures. However, the fundamental driving force can still be arterial dilation and contraction. Instead of having an accumulative effect on the ventricles, the force will be exerted locally at the perivascular space. The exact pathways of CSF

migration are not clear (Albargothy et al., 2018). Nevertheless, the close underlying coupling between vessel volume changes and CSF flow could contribute to multiple pathways.

4.3 Sleep vs. awake states

Previous research documents increases in the cortical interstitial space by more than 60% during sleep when compared with an awake condition, resulting in efficient convective clearance of β-amyloid and other compounds (Xie et al., 2013). This highly sleep-dependent clearance was observed in both human and mouse models (Bateman et al., 2006; Kang et al., 2009). In our study, we demonstrated a strong coupling between brain hemodynamics and CSF movement in awake participants. It suggests that CSF (albeit not robust) is maintained during the waking hours. It would be of great interest to understand the fundamental differences between sleep and the wakeful states, in term of vasomotion, CSF flow, coupling, and overall efficiency of clearance of the inflammatory proteins and metabolites.

Limitation and future studies.

There are several limitations to the study which we hope to address in future experiments. First, no respiration related data were collected, including chest belt and $P_{ET}CO_2$ measurements. These data can help us understand the physiological mechanisms of the LFOs in the fMRI. Second, we did not collect simultaneous EEG data. Thus, we could not confirm if the same neuro-vascular coupling as was demonstrated in the sleeping study, works in the wakeful state. Third, the net flow was not accurately assessed in this study. In future studies, we will incorporate respiration and EEG measurements. Moreover, we will compare the regular and forced breathing, to understand the differences in the underlying mechanisms.

Conclusions

A biomechanical model was proposed in this study to explain the delayed coupling between $\frac{d}{dt}$(GMS) and CSF flow. Two fMRI scans were conducted to validate our model and several predictions. We found 1) coupling existed between LFOs of $\frac{d}{dt}$(fMRI signal) and CSF flow signals when participants were awake; 2) the LFOs of $\frac{d}{dt}$(GMS) occurred about 2.2 seconds earlier than those of CSF inflow; 3) CSF flow at the fourth ventricle is bi-directional. Together, we conclude that the arterial LFO is the dominant force in driving CSF flow during wakefulness. These findings can help understand the mechanics of CSF flow and develop new interventions to increase the clearance rate in the brain, especially for patients with neurodegenerative diseases.

Reference

Aalling N, Munk ASF, Lundgaard I, Nedergaard M (2017) The Glymphatic System. SHORT COURSE:27.

Albargothy NJ, Johnston DA, MacGregor-Sharp M, Weller RO, Verma A, Hawkes CA, Carare RO (2018) Convective influx/glymphatic system: tracers injected into the CSF enter and leave the brain along separate periarterial basement membrane pathways. Acta neuropathologica 136:139-152.

Aldea R, Weller RO, Wilcock DM, Carare RO, Richardson G (2019) Cerebrovascular smooth muscle cells as the drivers of intramural periarterial drainage of the brain. Frontiers in aging neuroscience 11:1.

Asgari M, De Zélicourt D, Kurtcuoglu V (2016) Glymphatic solute transport does not require bulk flow. Scientific reports 6:38635.

Aslan S, Hocke L, Schwarz N, Frederick B (2019) Extraction of the cardiac waveform from simultaneous multislice fMRI data using slice sorted averaging and a deep learning reconstruction filter. Neuroimage 198:303-316.

Bateman RJ, Munsell LY, Morris JC, Swarm R, Yarasheski KE, Holtzman DM (2006) Human amyloid-β synthesis and clearance rates as measured in cerebrospinal fluid in vivo. Nature medicine 12:856-861.

Chen L, Beckett A, Verma A, Feinberg DA (2015) Dynamics of respiratory and cardiac CSF motion revealed with real-time simultaneous multi-slice EPI velocity phase contrast imaging. Neuroimage 122:281-287.

Delaidelli A, Moiraghi A (2017) Respiration: a new mechanism for CSF circulation? Journal of Neuroscience 37:7076-7078.

418 Diem AK, MacGregor Sharp M, Gatherer M, Bressloff NW, Carare RO, Richardson G (2017) Arterial
419 pulsations cannot drive intramural periarterial drainage: significance for Aβ drainage. Frontiers
420 in neuroscience 11:475.
421 Dreha-Kulaczewski S, Joseph AA, Merboldt K-D, Ludwig H-C, Gärtner J, Frahm J (2015) Inspiration is the
422 major regulator of human CSF flow. Journal of neuroscience 35:2485-2491.
423 Dreha-Kulaczewski S, Joseph AA, Merboldt K-D, Ludwig H-C, Gärtner J, Frahm J (2017) Identification of
424 the upward movement of human CSF in vivo and its relation to the brain venous system. Journal
425 of Neuroscience 37:2395-2402.
426 Dreha-Kulaczewski S, Konopka M, Joseph AA, Kollmeier J, Merboldt K-D, Ludwig H-C, Gärtner J, Frahm J
427 (2018) Respiration and the watershed of spinal CSF flow in humans. Scientific reports 8:1-7.
428 Duyn JH, Moonen CT, van Yperen GH, de Boer RW, Luyten PR (1994) Inflow versus deoxyhemoglobin
429 effects in BOLD functional MRI using gradient echoes at 1.5 T. NMR in Biomedicine 7:83-88.
430 Feinberg DA, Mark AS (1987) Human brain motion and cerebrospinal fluid circulation demonstrated with
431 MR velocity imaging. Radiology 163:793-799.
432 Fultz NE, Bonmassar G, Setsompop K, Stickgold RA, Rosen BR, Polimeni JR, Lewis LD (2019) Coupled
433 electrophysiological, hemodynamic, and cerebrospinal fluid oscillations in human sleep. Science
434 366:628-631.
435 Iliff JJ, Wang M, Zeppenfeld DM, Venkataraman A, Plog BA, Liao Y, Deane R, Nedergaard M (2013)
436 Cerebral arterial pulsation drives paravascular CSF–interstitial fluid exchange in the murine
437 brain. Journal of Neuroscience 33:18190-18199.
438 Jaeger E, Sonnabend K, Schaarschmidt F, Maintz D, Weiss K, Bunck AC (2020) Compressed-sensing
439 accelerated 4D flow MRI of cerebrospinal fluid dynamics. Fluids and Barriers of the CNS 17:1-11.
440 Jenkinson M, Beckmann CF, Behrens TE, Woolrich MW, Smith SM (2012) Fsl. Neuroimage 62:782-790.
441 Kang J-E, Lim MM, Bateman RJ, Lee JJ, Smyth LP, Cirrito JR, Fujiki N, Nishino S, Holtzman DM (2009)
442 Amyloid-β dynamics are regulated by orexin and the sleep-wake cycle. Science 326:1005-1007.
443 Klose U, Strik C, Kiefer C, Grodd W (2000) Detection of a relation between respiration and CSF pulsation
444 with an echoplanar technique. Journal of Magnetic Resonance Imaging 11:438-444.
445 Matsumae M, Kuroda K, Yatsushiro S, Hirayama A, Hayashi N, Takizawa K, Atsumi H, Sorimachi T (2019)
446 Changing the currently held concept of cerebrospinal fluid dynamics based on shared findings of
447 cerebrospinal fluid motion in the cranial cavity using various types of magnetic resonance
448 imaging techniques. Neurologia medico-chirurgica 59:133.
449 Mestre H, Tithof J, Du T, Song W, Peng W, Sweeney AM, Olveda G, Thomas JH, Nedergaard M, Kelley DH
450 (2018) Flow of cerebrospinal fluid is driven by arterial pulsations and is reduced in hypertension.
451 Nature communications 9:1-9.
452 Mokri B (2001) The Monro–Kellie hypothesis: applications in CSF volume depletion. Neurology 56:1746-
453 1748.
454 Nedergaard M (2013) Garbage truck of the brain. Science 340:1529-1530.
455 Power JD, Mitra A, Laumann TO, Snyder AZ, Schlaggar BL, Petersen SE (2014) Methods to detect,
456 characterize, and remove motion artifact in resting state fMRI. Neuroimage 84:320-341.
457 Schley D, Carare-Nnadi R, Please C, Perry V, Weller R (2006) Mechanisms to explain the reverse
458 perivascular transport of solutes out of the brain. Journal of theoretical biology 238:962-974.
459 Spijkerman JM, Geurts LJ, Siero JC, Hendrikse J, Luijten PR, Zwanenburg JJ (2019) Phase contrast MRI
460 measurements of net cerebrospinal fluid flow through the cerebral aqueduct are confounded by
461 respiration. Journal of Magnetic Resonance Imaging 49:433-444.
462 Telano LN, Baker S (2020) Physiology, Cerebral Spinal Fluid (CSF). StatPearls [Internet].
463 Tong Y, Yao J, Chen JJ, Frederick Bd (2019) The resting-state fMRI arterial signal predicts differential
464 blood transit time through the brain. Journal of Cerebral Blood Flow & Metabolism 39:1148-
465 1160.

466 Tong Y, Lindsey KP, Hocke LM, Vitaliano G, Mintzopoulos D, Frederick Bd (2017) Perfusion information
467 extracted from resting state functional magnetic resonance imaging. Journal of Cerebral Blood
468 Flow & Metabolism 37:564-576.
469 van Veluw SJ, Hou SS, Calvo-Rodriguez M, Arbel-Ornath M, Snyder AC, Frosch MP, Greenberg SM,
470 Bacskai BJ (2020) Vasomotion as a driving force for paravascular clearance in the awake mouse
471 brain. Neuron 105:549-561. e545.
472 Vigneau-Roy N, Bernier M, Descoteaux M, Whittingstall K (2014) Regional variations in vascular density
473 correlate with resting-state and task-evoked blood oxygen level-dependent signal amplitude.
474 Human brain mapping 35:1906-1920.
475 Wang P, Olbricht WL (2011) Fluid mechanics in the perivascular space. Journal of theoretical biology
476 274:52-57.
477 Xie L, Kang H, Xu Q, Chen MJ, Liao Y, Thiyagarajan M, O'Donnell J, Christensen DJ, Nicholson C, Iliff JJ
478 (2013) Sleep drives metabolite clearance from the adult brain. science 342:373-377.
479 Yamada S, Miyazaki M, Kanazawa H, Higashi M, Morohoshi Y, Bluml S, McComb JG (2008) Visualization
480 of cerebrospinal fluid movement with spin labeling at MR imaging: preliminary results in normal
481 and pathophysiologic conditions. Radiology 249:644-652.
482 Yamada S, Miyazaki M, Yamashita Y, Ouyang C, Yui M, Nakahashi M, Shimizu S, Aoki I, Morohoshi Y,
483 McComb JG (2013) Influence of respiration on cerebrospinal fluid movement using magnetic
484 resonance spin labeling. Fluids and barriers of the CNS 10:36.
485 Yang HC, Liang Z, Yao J, Shen X, Frederick Bd, Tong Y (2019) Vascular effects of caffeine found in BOLD
486 fMRI. Journal of neuroscience research 97:456-466.
487 Zhang Y, Brady M, Smith S (2001) Segmentation of brain MR images through a hidden Markov random
488 field model and the expectation-maximization algorithm. IEEE transactions on medical imaging
489 20:45-57.

490